



Published in final edited form as:

*Proc SPIE Int Soc Opt Eng.* 2018 March ; 10578: . doi:10.1117/12.2293879.

## Tests of clustering thalamic nuclei based on various dMRI models in the squirrel monkey brain

Yurui Gao<sup>\*,a,b</sup>, Kurt G. Schilling<sup>a,b</sup>, Iwona Stepniewska<sup>c</sup>, Junzhong Xu<sup>b,e</sup>, Bennett A. Landman<sup>a,b,d,e</sup>, Benoit M. Dawant<sup>a,d,e</sup>, and Adam W. Anderson<sup>a,b,e</sup>

<sup>a</sup>Biomedical Engineering, Vanderbilt University, Nashville, TN, USA 37235

<sup>b</sup>Institute of Imaging Science, Vanderbilt University, Nashville, TN, USA 37235

<sup>c</sup>Psychological Science, Vanderbilt University, Nashville, TN, USA 37235

<sup>d</sup>Electrical Engineering and Computer Science, Vanderbilt University, Nashville, TN, USA 37235

<sup>e</sup>Radiology and Radiological Sciences, Vanderbilt University, Nashville, TN, USA 37235

### Abstract

**Background**—Clustering thalamic nuclei is important for both research and clinical purposes. For example, ventral intermediate nuclei in thalami serve as targets in both deep brain stimulation neurosurgery and radiosurgery for treating patients suffering from movement disorders (e.g., Parkinson’s disease and essential tremor). Diffusion magnetic resonance imaging (dMRI) is able to reflect tissue microstructure in the central nervous system via fitting different models, such as, the diffusion tensor (DT), constrained spherical deconvolution (CSD), neurite orientation dispersion and density imaging (NODDI), diffusion kurtosis imaging (DKI) and the spherical mean technique (SMT).

**Purpose**—To test which of the above-mentioned dMRI models is better for thalamic parcellation, we proposed a framework of  $k$ -means clustering, implemented it on each model, and evaluated the agreement with histology.

**Method**—An *ex vivo* monkey brain was scanned in a 9.4T MRI scanner at 0.3mm resolution with  $b$  values of 3000, 6000, 9000 and 12000 s/mm<sup>2</sup>.  $K$ -means clustering on each thalamus was implemented using maps of dMRI models fitted to the same data. Meanwhile, histological nuclei were identified by AChE and Nissl stains of the same brain. Overall agreement rate and agreement rate for each nucleus were calculated between clustering and histology. Sixteen thalamic nuclei on each hemisphere were included.

**Results**—Clustering with the DKI model has slightly higher overall agreement rate but clustering with other dMRI models result in higher agreement rate in some nuclei.

**Conclusion**—dMRI models should be carefully selected to better parcellate the thalamus, depending on the specific purpose of the parcellation.

\* yurui.gao@vanderbilt.edu: phone:1-615-322-8359.

## Keywords

thalamic parcellation; diffusion MRI; dMRI modeling; clustering; deep brain stimulation; histology validation

---

## 1. INTRODUCTION

The thalamus is subdivided into a number of nuclei that possess functional specializations. Pinpointing thalamic nuclei is important for both research and clinical purposes. For example, the ventral intermediate nucleus (Vim) in the thalamus is a FDA-approved target in deep brain stimulation (DBS) neurosurgery [1, 2] and stereotactic radiosurgery [3, 4] performed on patients with Parkinson's disease (PD) symptoms or essential tremor (ET). Stimulating the Vim by implanted microelectrodes or destroying the Vim by radiation could alleviate tremor symptoms of the PD and ET patients. It is reported in non-human primates that microstructural characteristics (i.e., neuron size, neuron arrangement and fiber density) can be used to distinguish each nucleus from its neighbors [5]. For example, the VLp nucleus in monkey brain, homologous to the Vim in human, has large, multipolar neurons sparsely distributed between bundles of fibers.

Diffusion MRI (dMRI) is a noninvasive imaging method sensitive to the diffusion pattern of water molecules in brain tissue and thus is able to reflect local microstructural properties of neural tissue. Different diffusion models fit to the same dMRI signals emphasize different tissue properties: the diffusion tensor (DT [6]) characterizes the water diffusion profile in each voxel using a single 2<sup>nd</sup> order symmetric tensor [7]; constrained spherical deconvolution (CSD [8]) reconstructs multiple axon orientations in the same voxel in terms of spherical harmonics; neurite orientation dispersion and density imaging (NODDI [9]) estimates neurite density and orientation dispersion, diffusion kurtosis imaging (DKI [10]) measures diffusion profiles of tissue in terms of a higher order kurtosis tensor, and the spherical mean technique (SMT [11]) maps neurite density and microscopic diffusivities unconfounded by effects of orientation dispersion and crossing axons.

Previous studies reported using unsupervised clustering methods to parcellate the thalamus in human brain using maps derived from some of these dMRI models, such as the diffusion tensor [12] and orientation distribution [13], as features. However, clustering using other dMRI models has not been tested and the comparison among different models has not been investigated. Most importantly, evaluation of the clustering methods has not been performed in the same subjects using histology.

In our paper, a unified framework of  $k$ -means clustering for thalamic parcellation inspired by [12] is proposed. The framework is implemented on maps derived from each of the abovementioned dMRI models (i.e., DT, CSD, NODDI, DKI and SMT) in the squirrel monkey brain. Meanwhile, the histological thalamic nuclei in the same brain were identified on the basis of cytoarchitecture and myeloarchitecture. The agreement of each dMRI clustering with histological nuclei was evaluated in order to compare the performance of various dMRI models.

## 2. METHODS

The overall pipeline for our data acquisition, processing and analysis is graphically shown in Fig. 1. The squirrel monkey brain was scanned in a 9.4 Tesla MRI system to acquire high resolution multi-shell diffusion weighted images. The diffusion weighted images were preprocessed and then fit to five dMRI models (DT, CSD, NODDI, DKI and SMT). The  $k$ -means clustering algorithm was performed based on features calculated from each dMRI model. After the MRI scan, the monkey brain was sectioned, stained for Nissl and Acetylcholinesterase (AChE). The thalamic nuclei were outlined by an expert and then transformed into dMRI space. Finally, the agreement between each dMRI clustering and histology was evaluated. All animal procedures were approved by the Vanderbilt University Animal Care and Use Committee.

### 2.1 dMRI acquisition, model fitting and clustering

The fixed monkey brain was immersed in phosphate-buffered saline medium with 1mM Gd-DTPA in order to reduce longitudinal relaxation time [14]. After 2–3 weeks, the brain was placed in a container filled with liquid Fomblin and scanned in a 9.4 Tesla Agilent scanner (3D spin-echo EPI sequence with bipolar diffusion pulses, NSHOTS = 4, NEX = 1, TR = 410ms, TE = 41ms, voxel size = 0.3mm×0.3mm×0.3mm, data matrix = 128×192×128). The b-values for four shells were set to 3000, 6000, 9000 and 12000 s/mm<sup>2</sup>. Diffusion gradient duration and separation were 8ms and 22ms, respectively, for all the four shells. A gradient table of 107 uniformly distributed directions [15] was used as diffusion gradient directions for each shell. There were 3 b=0 scans interspersed among the 107 directions. Additionally, a single b=0 volume with reversed phase encoding direction was acquired immediately before each diffusion shell. The total scan time was approximately 50 hours.

FSL TOPUP [16] and EDDY [17] tools were used to correct susceptibility and eddy current-induced distortion and head movement on the raw diffusion data. Five dMRI models (DTI [6], CSD [8], NODDI [9], DKI [10] and SMT [11]) were implemented on the corrected data. The software used to fit the models and output maps of the models are listed in Table 1.

The left and right thalamus was manually segmented using ITK-SNAP software [18] ([www.itksnap.org](http://www.itksnap.org)). The lateral geniculate nucleus and medial geniculate nucleus were not included in the thalamus masks.

The commonly used  $k$ -means clustering algorithm in MATLAB was modified to cluster thalamic nuclei ( $k=16$ ) for each hemisphere. Inspired by the work of Wiegell et al [12], the distance metric  $d_{ik}$  between the  $i$ th thalamic voxel and the centroid of the  $k$ th thalamic cluster was defined as a linear combination of the normalized Mahalanobis spatial distance and the normalized Euclidean distance in dMRI parameter space, i.e.,

$$d_{ik} = \{Tr(W_X)\}^{-\frac{1}{2}} \|X_i - \bar{X}_k\|_{W_k} + \gamma \{Tr(W_P)\}^{-\frac{1}{2}} \|P_i - \bar{P}_k\|, \quad (1)$$

where  $X_i$  is the spatial location of the  $i$ th thalamic voxel,  $\bar{X}_k$  is the mean spatial location of the  $k$ th thalamic cluster,  $P_i$  is the vector composed of the given dMRI model output values at the  $i$ th thalamic voxel,  $\bar{P}_k$  is the mean vector of the dMRI output values of the  $k$ th cluster,  $W_X$  is the covariance matrix for spatial locations of all thalamic voxels, and  $W_P$  is the covariance matrix for dMRI output values of all thalamic voxels. The Mahalanobis distance is defined as

$$\|X_i - \bar{X}_k\|_{W_k} = \sqrt{(X_i - \bar{X}_k)^T W_k^{-1} (X_i - \bar{X}_k)}, \quad (2)$$

where  $W_k$  is the covariance matrix for the voxels in cluster  $k$ . The constant coefficients  $\{\text{Tr}(W_X)\}^{-1/2}$  and  $\{\text{Tr}(W_P)\}^{-1/2}$  are used for normalizing spatial distance and dMRI distance, respectively. The constant  $\gamma$  is the weighting factor to control the dMRI contribution and was kept the same across all the dMRI models. The cluster centroids for  $k$ -means were initialized by the center of mass for each histological nucleus in dMRI space. The clustering iteration was terminated when the maximum movement of the centroid is less than 0.1 of the voxel size (i.e., 0.03mm).

The clustering routine was repeated for a total of 100 trials and the initial centroid for each trial was shifted by a random distance uniformly distributed between 0 and 2 voxels (i.e., 0mm and 0.6mm). The maximum likelihood clustering result for each dMRI model was calculated by assigning the most frequent cluster label (out of 100 trials) to each thalamic voxel.

## 2.2 Histological nucleus identification and co-registration

After dMRI scanning, the brain was frozen and sectioned coronally at 50 $\mu$ m thickness using a microtome. The tissue blockface was photographed after sectioning every three sections by a camera rigidly mounted above the microtome. These blockface images were stacked in order, composing an intermediate space for registration from microscopy to dMRI space. One series of every sixth section was reacted for AChE and another series was reacted for Nissl. The two series of sections were both automatically photographed under a light microscope with 0.5 $\times$  magnification in the Digital Histology Shared Resource at Vanderbilt University. The borders of primary thalamic nuclei, 16 for each thalamus listed in Table 2, were identified and manually traced by a neuroanatomist with more than 20 years' experiences, based on micro-architectonics revealed by the AChE and Nissl stains [5]. The manual tracing of each thalamic nucleus was aligned with AChE microscopy and binarized. The binary mask of each thalamic nucleus was transformed to dMRI space using deformation fields calculated via a multi-step registration procedure, which included 2D affine and nonlinear registration [19] from light microscopy to the corresponding blockface image (one slice at a time) and then 3D affine and nonlinear registration from the blockface stack to dMRI volume (see [20–22] for more details). The 16 thalamic nuclei we identified are listed in Table 2 [5].

### 2.3 Comparison of dMRI clustering and histology

To evaluate overall agreement of parcellation, we calculated the Jaccard index for all nuclei, defined as  $R_a$ . To evaluate agreement for each parcellated nucleus, we calculated the Jaccard index for each nucleus, defined as  $r_a$ . Both  $R_a$  and  $r_a$  indicate how many out of the total number of voxels were correctly clustered. The average and standard deviation of  $R_a$  and  $r_a$  were calculated from 100 trials of  $k$ -means clustering (as described in part 2.1) for each of the five dMRI models.

## 3. RESULTS

Figure 2 shows the dorsal views of dMRI clustering results and histological parcellation in the same dMRI space. Each panel of fig. 2A–2E shows the maximum likelihood clustering calculated from 100 trials of  $k$ -means clustering using the given dMRI model.

Figure 3A–E illustrate the average and standard deviation of the 100 trials of agreement rates,  $r_a$ , between histology and  $k$ -means clustering for each dMRI model, i.e., DT (Fig. 3A), CSD (Fig. 3B), NODDI (Fig. 3C), DKI (Fig. 3D), and SMT (Fig. 3E), for each individual nucleus in the left hemisphere (blue bar) and right hemisphere (yellow bar). Figure 3F lists the average and standard deviation of overall agreement rate,  $R_a$ . The average of  $R_a$  is in the range of 0.45–0.67.

## 4. DISCUSSION

This paper proposes a  $k$ -means clustering framework to parcellate the thalamus by integrating microstructural properties of tissue estimated from dMRI models. The method was implemented using five dMRI models and evaluated by comparing with histological parcels in the same monkey brain. In figure 2, DKI shows slightly higher overall agreement with histology and SMT shows significantly lower agreement than other dMRI models. However, the order of overall agreement,  $R_a$ , does not necessarily align with the order of agreement  $r_a$ . For example, CSD gives highest  $r_a$  with respect to the VLP nucleus in monkey brain. Note that VLP in monkey brain corresponds to VIM in the human. The Euclidean distance between diffusion measures, as shown in Eq.(1), equally weighted each component in the parameter set for the dMRI model. Based on our previous work [23], these components might contribute differently to clustering. So we will improve our  $k$ -means clustering in the future by adding appropriate weighting factors.

## Acknowledgments

This work was supported by NIH grants R01NS058639 and R01NS095291. The work was also supported by a pilot grant from the Vanderbilt Institute for Surgery and Engineering (VISE). We also thank the Advanced Computing Center for Research and Education (ACCRE) and Digital Histology Shared Resource (DHSR) at Vanderbilt University.

## References

1. Benabid AL, Pollak P, Louveau A, et al. Combined (thalamotomy and stimulation) stereotactic surgery of the {VIM} thalamic nucleus for bilateral {Parkinson} disease. *Applied Neurophysiology*. 1987; 50(1–6):344–346. [PubMed: 3329873]

2. Benabid AL, Pollak P, Gao D, et al. Chronic electrical stimulation of the ventralis intermedius nucleus of the thalamus as a treatment of movement disorders. *Journal of Neurosurgery*. 1996; 84(2):203–214. [PubMed: 8592222]
3. Young RF, Shumway-Cook A, Vermeulen SS, et al. Gamma knife radiosurgery as a lesioning technique in movement disorder surgery. *Journal of Neurosurgery*. 1998; 89(2):183–193. [PubMed: 9688111]
4. Luo G, Neimat JS, Cmelak AJ, et al. Margin of Error for a Frameless Image Guided Radiosurgery System: Direct Confirmation Based on Posttreatment MRI Scans. *International Journal of Radiation Oncology • Biology • Physics*. 2015; 93(3):S84.
5. Stepniewska I, Preuss TM, Kaas JH. Architectonic subdivisions of the motor thalamus of owl monkeys: Nissl, acetylcholinesterase, and cytochrome oxidase patterns. *The Journal of Comparative Neurology*. 1994; 349(4):536–557. [PubMed: 7860788]
6. Basser PJ, Mattiello J, Lebihan D. MR diffusion tensor spectroscopy and imaging. *Biophysical Journal*. 1994; 66(1)
7. Pierpaoli C, Jezzard P, Basser PJ, et al. Diffusion tensor MR imaging of the human brain. *Radiology*. 1996; 201:637–648. [PubMed: 8939209]
8. Tournier JD, Yeh CH, Calamante F, et al. Resolving crossing fibres using constrained spherical deconvolution: Validation using diffusion-weighted imaging phantom data. *Neuroimage*. 2008; 42(2):617–625. [PubMed: 18583153]
9. Zhang H, Schneider T, Wheeler-Kingshott CA, et al. NODDI: Practical in vivo neurite orientation dispersion and density imaging of the human brain. *NeuroImage*. 2012; 61(4):1000–1016. [PubMed: 22484410]
10. Jensen JH, Helpert JA, Ramani A, et al. Diffusional kurtosis imaging: The quantification of non-gaussian water diffusion by means of magnetic resonance imaging. *Magnetic Resonance in Medicine*. 2005; 53(6):1432–1440. [PubMed: 15906300]
11. Kaden E, Kelm ND, Carson RP, et al. Multi-compartment microscopic diffusion imaging. *NeuroImage*. 2016; 139:346–359. [PubMed: 27282476]
12. Wiegell MR, Tuch DS, Larsson HBW, et al. Automatic segmentation of thalamic nuclei from diffusion tensor magnetic resonance imaging. *NeuroImage*. 2003; 19(2):391–401. [PubMed: 12814588]
13. Battistella G, Najdenovska E, Maeder P, et al. Robust thalamic nuclei segmentation method based on local diffusion magnetic resonance properties. *Brain Structure & Function*. 2017; 222(5):2203–2216. [PubMed: 27888345]
14. D’Arceuil HE, Westmoreland S, de Crespigny AJ. An approach to high resolution diffusion tensor imaging in fixed primate brain. *NeuroImage*. 2007; 35(2):553–565. [PubMed: 17292630]
15. Caruyer E, Lenglet C, Sapiro G, et al. Design of multishell sampling schemes with uniform coverage in diffusion MRI. *Magnetic Resonance in Medicine*. 2013; 69(6):1534–1540. [PubMed: 23625329]
16. Andersson JLR, Skare S, Ashburner J. How to correct susceptibility distortions in spin-echo echo-planar images: application to diffusion tensor imaging. *NeuroImage*. 2003; 20(2):870–888. [PubMed: 14568458]
17. Andersson JLR, Sotiropoulos SN. An integrated approach to correction for off-resonance effects and subject movement in diffusion MR imaging. *NeuroImage*. 2016; 125:1063–1078. [PubMed: 26481672]
18. Yushkevich PA, Piven J, Hazlett HC, et al. User-guided 3D active contour segmentation of anatomical structures: Significantly improved efficiency and reliability. *NeuroImage*. 2006; 31(3): 1116–1128. [PubMed: 16545965]
19. Rohde GK, Aldroubi A, Dawant BM. The adaptive bases algorithm for intensity-based nonrigid image registration. *IEEE Transactions on Medical Imaging*. 2003; 22(11):1470–1479. [PubMed: 14606680]
20. Choe A, Gao Y, Li X, et al. Accuracy of image registration between MRI and light microscopy in the ex vivo brain. *Magnetic Resonance Imaging*. 2011; 29(5):683–692. [PubMed: 21546191]

21. Gao Y, Choe AS, Stepniewska I, et al. Validation of DTI Tractography-Based Measures of Primary Motor Area Connectivity in the Squirrel Monkey Brain. *PLoS one*. 2013; 8(10):e75065. [PubMed: 24098365]
22. Gao Y, Schilling KG, Stepniewska I, et al. Tests of cortical parcellation based on white matter connectivity using diffusion tensor imaging. *NeuroImage*. 2017
23. Gao Y, Schilling K, Stepniewska I, et al. Validation of DTI-based parcellation of the thalamus in the squirrel monkey; *Proceeding of ISMRM*; Honolulu, Hawaii. 2017.



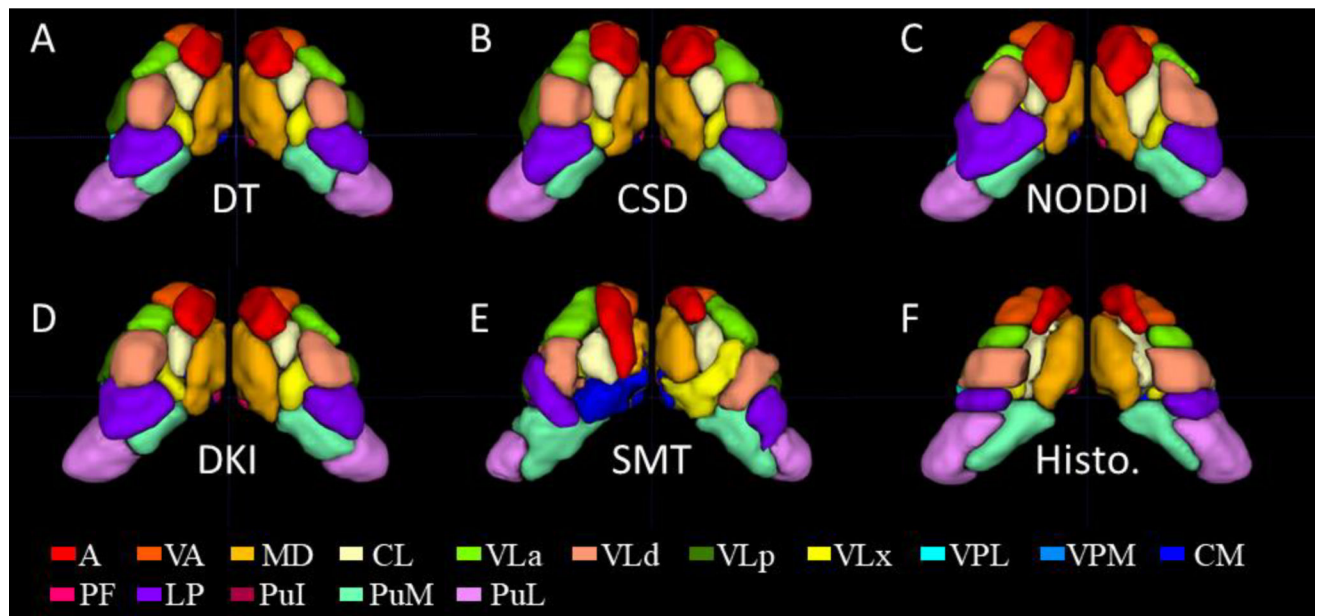


**Figure 2.**

Dorsal view of  $k$ -means clustering of each dMRI model and the histological parcels in the same monkey brain. (A)–(E) show maximum likelihood clustering results from 100 trials of  $k$ -means clustering using five dMRI models: DT, CSD, NODDI, DKI and SMT. (F) shows the histological parcels identified on the basis of AChE and Nissl stained micro-architectonics.

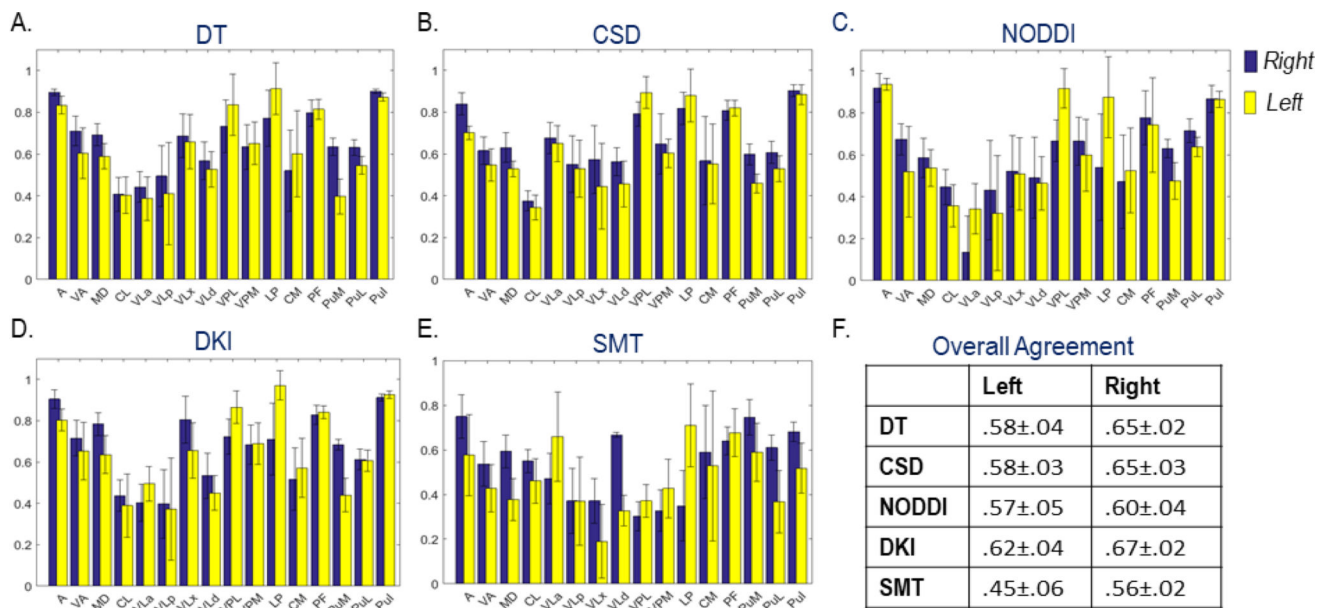


**Figure 3.**

Agreement rates,  $r_a$  and  $R_a$ , between dMRI clustering and histological ground truth. (A)–(E) show the agreement rate,  $r_a$ , for each individual nucleus between histology and  $k$ -means clustering using five diffusion models: DT, CSD, NODDI, DKI and SMT. Solid bars and error bars represent the average and standard deviation of  $r_a$  distribution obtained from 100 trials of  $k$ -means clustering. (F) displays the overall agreement rate,  $R_a$ , over the entire thalamus between histology and clustering.

**Table 1**

List of dMRI models, corresponding software tools and output maps.

<b>dMRI Model</b>	<b>Software Tool</b>	<b>Output Maps</b>
<b>DTI</b> [6]	FSL Diffusion Tool <a href="https://fsl.fmrib.ox.ac.uk">https://fsl.fmrib.ox.ac.uk</a>	$D_{i,j}$ – components of diffusion tensor ( $i, j = 1, 2, 3$ )
<b>CSD</b> [8]	MRtrix3 <a href="http://www.mrtrix.org">www.mrtrix.org</a>	$c_j$ – coefficients of spherical harmonics ( $j = 1, 2, \dots, 45$ )
<b>NODDI</b> [9]	NODDI toolbox <a href="http://www.nitrc.org/projects/noddi_toolbox">www.nitrc.org/projects/noddi_toolbox</a>	$v_{ic}$ – apparent intra-cellular volume fraction $v_{iso}$ – apparent CSF volume fraction $od$ – orientation dispersion index $V$ – main fiber bundle orientation
<b>DKI</b> [10]	DKE <a href="http://www.nitrc.org/projects/dke">www.nitrc.org/projects/dke</a>	$D_{i,j,k,l}$ – components of kurtosis tensor ( $i, j, k, l = 1, 2, 3$ )
<b>SMT</b> [11]	SMT tool <a href="https://github.com/ekaden/smt">https://github.com/ekaden/smt</a>	$v_{in}$ – apparent intra-neurite volume fraction; $D_{in}$ – intrinsic intra-neurite diffusivity

**Table 2**

List of 16 thalamic nuclei in each hemisphere of the squirrel monkey brain.

	Nucleus		Nucleus		Nucleus		
<b>A</b>	Anterior	<b>VLa</b>	Ventrolateral anterior	<b>VPL</b>	Ventral posterolateral	<b>LP</b>	Lateral posterior
<b>VA</b>	Ventral anterior	<b>VLd</b>	Ventrolateral dorsal	<b>VPM</b>	Ventral posteromedial	<b>PuI</b>	Pulvinar inferior
<b>MD</b>	Median dorsal	<b>VLp</b>	Ventrolateral posterior	<b>CM</b>	Central medial	<b>PuM</b>	Pulvinar medial
<b>CL</b>	Central laminar	<b>VLx</b>	Ventrolateral medial	<b>PF</b>	Parafascicular	<b>PuL</b>	Pulvinar lateral